



Numerical investigation of heat, flow and particle trajectory in A-TIG welding pool of 304L-SS

Sara Pourmand¹ · Amin Ramiani Jafari¹ · Alireza Ebrahimi¹

Received: 29 February 2020 / Accepted: 8 September 2020 / Published online: 17 September 2020
© International Institute of Welding 2020

Abstract

A three-dimensional CFD-model was developed to investigate Active-TIG welding of 304L-SS, involving heat transfer, fluid flow, solidification, plasma arc effect, Marangoni convections, magnetohydrodynamics and oxide particle trajectory. The aim was to understand how flux-induced particles are distributed in the weld line. The results, validated with available experimental data, showed that A-TIG forms a pool with an increased maximum temperature (2800 K) and depth-to-width ratio (0.7). The flow pattern, dominated by two vortices due to Marangoni convection, collects particles from the surface, submerges them into the pool and leads to entrapment of the most in the weld cross section. The motion path of 70% of particles ended at the deeper half of the cross section. Detailed numerical picture of A-TIG weld pool was presented and discussed in this study to be a step in understanding of the nature of Active-TIG welding and to assist in improving the process.

Keywords A-TIG welding · CFD · Solidification · Marangoni flow · Particle trajectory · Magnetohydrodynamics

1 Introduction

Tungsten inert gas (TIG) is a common fabrication process for stainless steel products for its good-quality welds. The process is mainly concerned with a weld pool of molten metal, formed by heat source of the plasma arc, which itself is associated with multi-physics of melt flow, heat and mass transport, melting/solidification, metallurgical structure evolutions, oxidation/reduction, thermo-capillary effects and magnetohydrodynamic interactions. Therefore, the weld pool essentially determines the performance of welding and the characteristics of the final joint. Though from experiments, it was seen that the weld pool goes undersized in depth when it comes to joint thick sections. Paton welding institute proposed to apply a covering of oxide-flux on the surface of thick-sectioned pieceworks and made a significant improvement in the depth of welding, named Active-TIG [1]. Modenesi et al. [2] approved that all kinds of

fluxes change the weld pool and increase the penetration depth. Heiple and Roper [3] gave two hypotheses for that effect, arc contraction and inversion of Marangoni flow due to chemical change in top layers of melt. Marangoni flow is driven by unbalanced surface tension at points on top of the weld pool because of high gradient in temperature distribution. Using mathematical simulations, Zhao et al. [4] have demonstrated internal vortexes in the pool formed by surface tension effects. Beside the presence of high-temperature gradients, variations of surface tension with sulphur and oxygen content have also been reported to originate intense thermo-capillary flows which alters the direction of circulations in the weld pool [5]. For A-TIG, Li et al. [6] reported narrow and deep weld pool shape with inward Marangoni flow. Li et al. [7] found that surface tension can reach to a maximum value with increasing the thickness of flux coating. Wang et al. [8] conducted a coupled modelling of weld pool and plasma arc for TIG and A-TIG while there was an equal amount of heat input for both, implying that a deeper pool is not an effect of the arc. The investigations have revealed that the inversion of Marangoni flow is more likely to be the mechanism of increasing the penetration depth of A-TIG joints. With mathematical modelling, Zhao et al. [4] have predicted the effect of oxygen content on the flow pattern and intensity of melt circulations in the pool. Berthier et al. [9] also demonstrated the effect of different activating oxide-flux on the weld pool via a two-dimensional

Recommended for publication by Study Group 212 - The Physics of Welding

✉ Amin Ramiani Jafari
ajafari@aut.ac.ir

¹ Department of Materials and Metallurgical Engineering, Amirkabir University of Technology (Tehran Polytechnic), No.424 Hafez St, Tehran 15916-34311, Iran

axisymmetric simulation. Although Active-TIG has shown promising results aiming an enhanced penetration, its application have been prone to shortages. Vidiyarthi and Dwivedi [10] have reviewed issues in A-TIG. The oxide particles of the covering flux may be immersed (plunged) into the molten pool and trapped in the weld line [11]. Since entrapped particles can turn to sites of crack nucleation, they facilitate fracture and degrade the mechanical properties of the joint in a form of lower resistance to fatigue, tensile strength and elongation. Having knowledge on the movement of flux particles within the pool would assist to improve the quality of the weld. Based on SEM metallographic images, Feyzi [12] measured surface fraction, diameter and number density of oxide particles. Aucott et al. [11] used synchrotron X-ray imaging to capture, visualize and quantify in situ melt pool evolutions in real metallic alloys. They indicated the occurrence of surface turbulent flow which can drag small oxide particles into the pool. They also confirmed the suggested mechanism for the change in shape of the fusion zone, pointing that changing the steel composition from low sulphur to high sulphur not only changes the flow direction but also increases the flow velocities and melt pool dimensions.

Modelling of welding process deals with description of multiphase fluid flow, heat transport, mass transport, arc electromagnetics, phase change, thermodynamics, kinetics and movement of free-floating particles. As an example, Jaidi and Dutta [13] have conducted a simulation concentrating on flow phenomena in the welding pool. In another attempt, Yushchenko et al. [14] modelled heat flow and magnetohydrodynamic effects of a stationary arc. Multiphase models are capable of handling coupled transports of liquid, solid and floating particles, referring to Eulerian-Eulerian approach [15]. In metallurgical systems however, the effects of particle movements on the flow field are neglected frequently, where the oxide particles have small volumes and densities, with respect to those of system dimensions and melt properties. Therefore, particle motion is regularly simplified with uncoupled Eulerian-Lagrangian approach in the metallurgical processes [16], i.e. the fluid flow, assumed to be undisturbed by particles, is simulated in the first place, and then an equation of motion is used for solid particles, e.g. Stokes law, to calculate their paths within the flow field. An important aspect is the drag force experienced by the particle, which depends on particle morphology, fluid viscosity and local relative velocity of the particle with respect to fluid flow [17]. Another issue in simulations of A-TIG welding deals with the modelling of surface tension-driven flow. While the Marangoni effect is described as a sharp shear stress on the free surface of the fluid, attentions should be drawn to the very shallow layers of the fluid at top surface. Modelling of the boundary layer just beneath the surface may demand very fine grid spacing and much more modelling attempts to catch the real velocity profile [18]. Furthermore, all these have to be coupled together with a solidification/melting phase change model that

considers mushy flow near the wall of weld pool. In this research, a process of A-TIG welding is considered to be investigated for its weld pool geometry, temperature distribution, velocity field and oxide particle motion path. Therefore, a comprehensive numerical setup was developed to compute dependent variables consisting velocity, enthalpy, temperature and solid-liquid fractions in the metallic system and subsequently the velocity and position of oxide particles as a function of space and time.

2 Mathematical model

Fully realistic modelling of the welding could be extremely complicated, since it involves multi-physics related to plasma arc, radiations, material evolutions, chemical reactions, weld pool dynamics and magnetohydrodynamics, as well as the transport phenomena of heat, mass, momentum and electric charge [19]. In this paper, however, we are focused on the objective of the current study, which is to investigate the distribution of oxide particles within A-TIG weld pool. It can thus be reasonable to outline and to simplify the problem with some assumptions as much as the main effects are remained related to the objective. Figure 1 illustrates the calculation domain and boundary surfaces. For the plane symmetry of the weld line, only one-half of the workpiece is taken as the calculation domain which is $50 \times 10 \times 30 \text{ mm}^3$ along length (x), thickness (y) and width (z) of the sheet, respectively.

The following assumptions were made to describe the process: (a) The process has essentially three-dimensional transports. (b) The weld is assumed to be plane-symmetrical on two sides of the weld center line. (c) The mathematical model is chosen to be transient to facilitate numerical convergence from a pseudo-initial condition (time relaxation). However, as the frame of reference is attached to the welding torch (i.e. sheet metal enters the domain from one side and leaves from the other side), the final solution is considered to be steady-state. (d) The top surface of the welded joint was assumed to be flat. (e) Molten metal is a Newtonian and incompressible fluid (f) The fluid flow is turbulent; however, turbulent effects

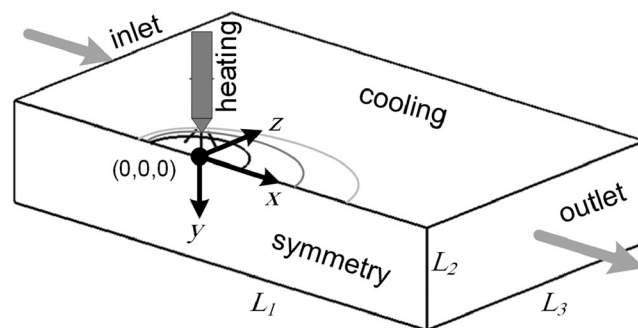


Fig. 1 Computational domain (half workpiece) with the frame of reference attached to the welding torch

Table 1 The boundary conditions used in the present model

Boundaries	Position	Temperature	Velocity
Initial condition, $t = 0$	$-L_1/2 \leq x \leq L_1/2$	$T = T_o$	$u = u_w, v = 0, w = 0$
Top	$0 \leq y \leq L_2, 0 \leq z \leq L_3$ $-L_1/2 \leq x \leq L_1/2$	$\frac{\partial T}{\partial y} = -\frac{q_{arc} + q_{air}}{k}$	$\frac{\partial u}{\partial x} = 0, v = 0, \frac{\partial w}{\partial z} = 0$
Bottom	$y = 0, 0 \leq z \leq L_3$ $-L_1/2 \leq x \leq L_1/2$	$\frac{\partial T}{\partial y} = -\frac{q_{air}}{k}$	$u = u_w, v = 0, w = 0$
Symmetry	$y = L_2, 0 \leq z \leq L_3$ $-L_1/2 \leq x \leq L_1/2$	$\frac{\partial T}{\partial z} = 0$	$\frac{\partial u}{\partial z} = 0, v = 0, w = 0$
Inlet	$0 \leq y \leq L_2, z = 0$ $x = -L_1/2$	$T = T_o$	$u = u_w, v = 0, w = 0$
Outlet	$0 \leq y \leq L_2, 0 \leq z \leq L_3$ $x = L_1/2$	$\frac{\partial T}{\partial x} = 0$	$\frac{\partial u}{\partial x} = 0, v = 0, w = 0$

were considered via effective material parameters in a laminar model. (g) It is assumed that the electric power of arc welding exposes the top surface with a Gaussian distribution. (h) The only difference between TIG and A-TIG welding processes is considered to be the presence of a covering flux and free motion of oxide particles in the weld pool of A-TIG. (g) The thickness of the covering flux in A-TIG is ignorable compared with the dimensions of the welding pool. The flux layer in A-TIG only changes the surface energy gradients of the molten metal. All other parameters are the same for both of the processes.

Table 2 Material properties used in mathematical model for stainless steel 304L. The value of surface tension gradients for TIG and A-TIG are adopted from ref. [12, 28]

Properties/parameters	Symbol	Value	Unit
Density	ρ	7200	kg/m ³
Viscosity	μ	0.006	kg/ms
Specific heat capacity	c	600	J/kgK
Thermal conductivity	k	35	W/mK
Latent heat of fusion	L_f	245	kJ/kg
Solidus temperature	T_s	1645	K
Liquidus temperature	T_L	1672	K
Porosity constant	K_o	6.67×10^{-11}	m ²
Effective arc radius	r_o	3	mm
Welding voltage	V	15	V
Welding current	I	150	A
Welding speed	u_w	0.005	m/s
Arc efficiency	η	70%	-
Magnetic permeability	μ_m	1.26×10^{-6}	H/m
Surface tension gradient	$\partial\gamma/\partial T$		
TIG		-10^{-4}	N/mK
A-TIG (low oxygen)		10^{-4}	N/mK
A-TIG (high oxygen)		5×10^{-4}	N/mK

The governing equations used in the model are continuity, momentum and energy equations in three dimensions based on the conservation principles as following [20]:

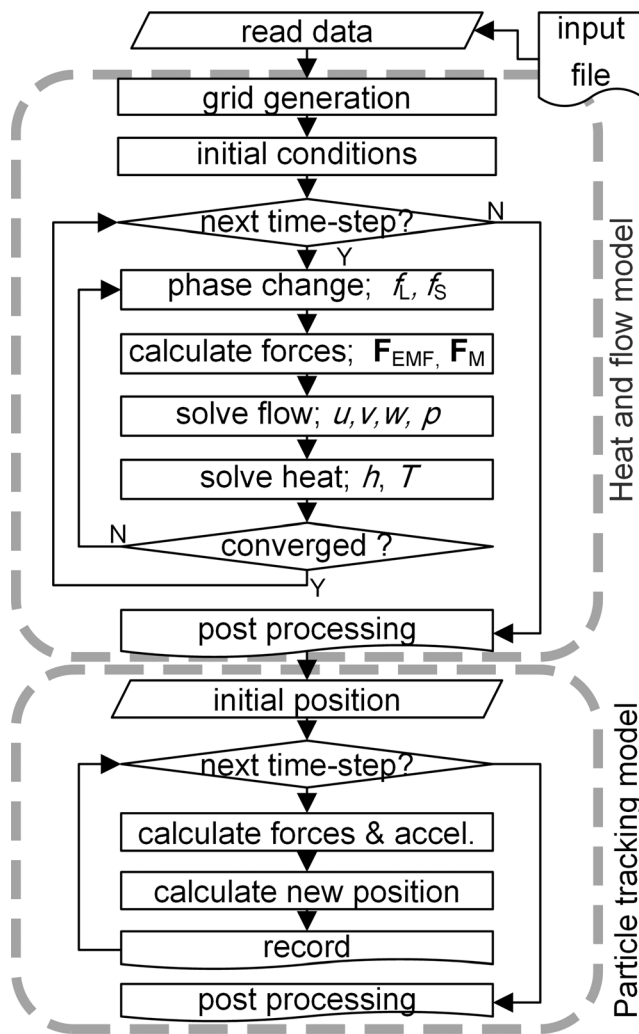


Fig. 2 Algorithm of the numerical model and computations for particle trajectory in the weld pool

$$\frac{\partial \rho}{\partial t} + \frac{\partial(\rho u)}{\partial x} + \frac{\partial(\rho v)}{\partial y} + \frac{\partial(\rho w)}{\partial z} = 0 \quad (1)$$

$$\begin{aligned} & \frac{\partial(\rho u)}{\partial t} + \frac{\partial(\rho uu)}{\partial x} + \frac{\partial(\rho uv)}{\partial y} + \frac{\partial(\rho uw)}{\partial z} \\ & = \mu_{\text{eff}} \left(\frac{\partial^2 u}{\partial x^2} + \frac{\partial^2 u}{\partial y^2} + \frac{\partial^2 u}{\partial z^2} \right) - \frac{\partial P}{\partial x} + F_x^{\text{EMF}} + F_x^{\text{D}} \end{aligned} \quad (2)$$

$$\begin{aligned} & \frac{\partial(\rho v)}{\partial t} + \frac{\partial(\rho vu)}{\partial x} + \frac{\partial(\rho vv)}{\partial y} + \frac{\partial(\rho vw)}{\partial z} \\ & = \mu_{\text{eff}} \left(\frac{\partial^2 v}{\partial x^2} + \frac{\partial^2 v}{\partial y^2} + \frac{\partial^2 v}{\partial z^2} \right) - \frac{\partial P}{\partial y} + F_y^{\text{M}} + F_y^{\text{EMF}} + F_y^{\text{D}} \end{aligned} \quad (3)$$

$$\begin{aligned} & \frac{\partial(\rho w)}{\partial t} + \frac{\partial(\rho wu)}{\partial x} + \frac{\partial(\rho wv)}{\partial y} + \frac{\partial(\rho ww)}{\partial z} \\ & = \mu_{\text{eff}} \left(\frac{\partial^2 w}{\partial x^2} + \frac{\partial^2 w}{\partial y^2} + \frac{\partial^2 w}{\partial z^2} \right) - \frac{\partial P}{\partial z} + F_z^{\text{M}} + F_z^{\text{EMF}} \end{aligned} \quad (4)$$

$$\begin{aligned} & \frac{\partial(\rho h)}{\partial t} + \frac{\partial(\rho uh)}{\partial x} + \frac{\partial(\rho vh)}{\partial y} + \frac{\partial(\rho wh)}{\partial z} \\ & = \frac{k_{\text{eff}}}{c} \left(\frac{\partial^2 h}{\partial x^2} + \frac{\partial^2 h}{\partial y^2} + \frac{\partial^2 h}{\partial z^2} \right) + S^h \end{aligned} \quad (5)$$

The viscosity and thermal conductivity of melt have been replaced by their approximate effective values [21] to roughly account for turbulent effects. The source terms are introduced in the momentum equations describing electromagnetic force, solid-liquid mush damping and Marangoni effects. In the energy equation, the source term S^h is responsible for melting/solidification latent heat effects. Neglecting heat of mechanical works, total enthalpy consists of latent heat and sensible heat as $h_{\text{total}} = h^{\text{ref}} + \int_{T_{\text{ref}}}^T c dT$. Latent heat, i.e. the reference enthalpy, is evaluated for the two-phase solid-liquid mixture as $h^{\text{ref}} = f_S h_S^{\text{ref}} + f_L h_L^{\text{ref}} \approx f_L L_f$, considering the base value (zero) for solid. Mass fraction of liquid f_L is calculated iteratively as a linear state function of temperature within the solidification range between liquidus of solidus temperatures. The source term F^{M} in Eqs. (3) and (4) is volume-averaged Marangoni force due to surface tension gradients. The surface tension gradient is the parameter that determines the difference between TIG and A-TIG welding. The values of the parameter are listed in Table 2. The Marangoni effect is frequently applied to the boundary condition, as used by Wang et al. [8]. However, the thermosolutal Marangoni boundary layer demands very fine grid spacing and much more modelling attempts to find an accurate velocity profile as mentioned by Pop et al. [22]. To overcome the issue in this study, the Marangoni shear stress was converted to a volume-averaged Marangoni volumetric force assuming a linear velocity profile in the boundary layer. The volume-averaged force was then applied to just the first row

of surface volume elements in the momentum equation, that assists to avoid extra numerical attempts to refine the grid and to capture the Marangoni boundary layer. The phase change region is considered to be a rigid and porous dendritic structure of solid metal through which the molten metal is flowing. Therefore, the shear stress on the solid-liquid interface is modelled by Darcy damping source term, assuming an

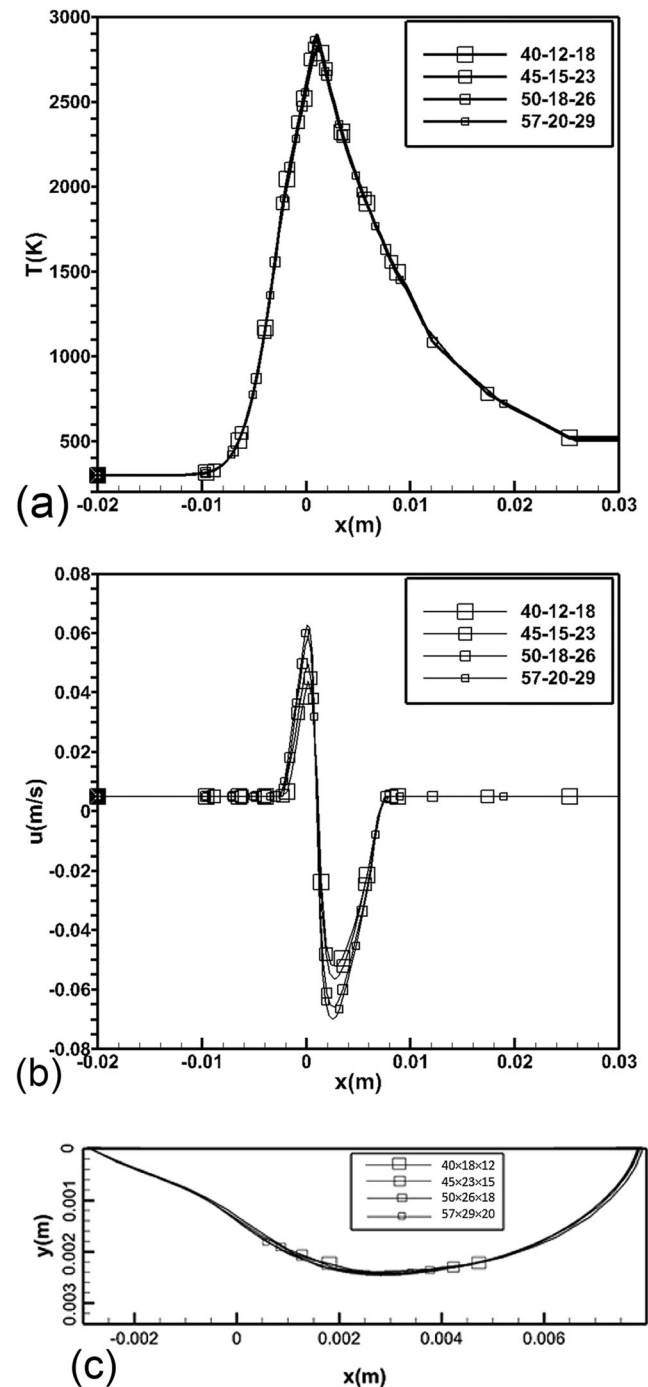
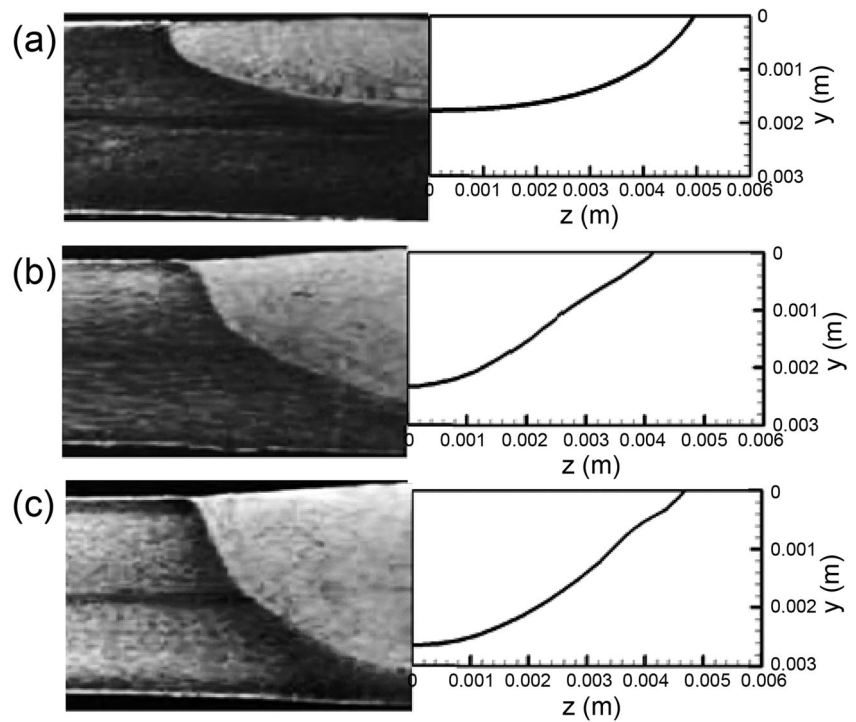


Fig. 3 Numerical results for grid dependency study. **a** Temperature distribution on the weld line. **b** Velocity changes in the x direction on the weld line. **c** Geometry of the pool in the longitudinal section

Fig. 4 Geometry of A-TIG welding pool with different oxygen percentage in cross section. Right: the result obtained from the present numerical model, left: the experimental results by Tseng and Hsu [29]. **a** Without flux, $\partial\gamma/\partial T = -10^{-4}$ (N/mK). **b** With medium oxygen content, $\partial\gamma/\partial T = 10^{-4}$ (N/mK). **c** With high oxygen content, $\partial\gamma/\partial T = 5 \times 10^{-4}$ (N/mK)



isotropic permeability [23]. Electromagnetic effect of plasma arc on the flow regime has been introduced via Lorentz’s force in the momentum Eqs. (2)–(4). It is intrinsically defined as $\mathbf{F}^{EMF} = \mathbf{J} \times \mathbf{B}$ and therefore, an approximated formulation for \mathbf{F}^{EMF} by Kumar and Debroy [24] was adopted to be used in this study, assuming that the flow pattern does not affect the electromagnetic field. According to the explanation of the model, the additional terms and equations required to close the mathematical model are summarized as following:

$$F_x^{EMF} = -\frac{\mu_m I^2}{4\pi^2 r_0^2 r} \exp\left(-\frac{r}{2r_0^2}\right) \left[1 - \exp\left(-\frac{r}{2r_0^2}\right)\right] \left[1 - \left(\frac{y}{L_3}\right)\right]^2 \frac{x}{r} \quad (6)$$

$$F_y^{EMF} = \frac{\mu_m I^2}{4\pi^2 r^2 c} \left[1 - \exp\left(-\frac{r}{2r_0^2}\right)\right]^2 \left[1 - \left(\frac{y}{L_3}\right)\right] \quad (7)$$

$$F_z^{EMF} = -\frac{\mu_m I^2}{4\pi^2 r_0^2 r} \exp\left(-\frac{r}{2r_0^2}\right) \left[1 - \exp\left(-\frac{r}{2r_0^2}\right)\right] \left[1 - \left(\frac{y}{L_3}\right)\right]^2 \frac{z}{r} \quad (8)$$

$$F_x^M = \frac{\partial\gamma}{\partial T} \frac{\partial T}{\partial x}, F_z^M = \frac{\partial\gamma}{\partial T} \frac{\partial T}{\partial z} \quad (9)$$

$$F^D = -\frac{\mu}{K} (v - v_s), K = K_0 \frac{\varepsilon_L^3}{(1 - \varepsilon_L)^2} \quad (10)$$

$$S^h = -\rho L_f \left[\frac{\partial f_L}{\partial t} + \frac{\partial(f_L u)}{\partial x} + \frac{\partial(f_L v)}{\partial y} + \frac{\partial(f_L w)}{\partial z} \right] \quad (11)$$

$$f_L = \begin{cases} 1 & T \geq T_L \\ (T - T_s)/(T_L - T_s) & T_s < T < T_L \\ 0 & T \leq T_s \end{cases} \quad (12)$$

The A-TIG welding process, with a covering flux that produces oxide particles, involves free motion of the oxide particles within the melt pool. Therefore, the model is also required to describe the phenomenon with a set of particle tracking formulations. This part of the model works only for A-TIG simulations and it is turned off for the TIG process. The particle tracking model, based on Newton’s motion law that reads $\sum F_p = ma$, involves forces acting on the particles. Two major forces in particle dynamics are Stokes’ drag force and gravity force. The drag force experienced by the particle is proportional to the difference between the particle velocity and the undisturbed fluid velocity prior to the introduction of the particle at the same location [25]. The particle tracking model can be summarized to following equations:

$$m \frac{d^2x}{dt} = F_G + F_D \quad (13)$$

$$F_D = 3\pi\mu D(v - v_p) \quad (Re_p < 1000) \quad (14)$$

$$F_G = \frac{\pi}{6} \left(\frac{\rho_p - \rho}{\rho_p} \right) g D^3 \quad (15)$$

As the flow field is computed, it is used to calculate motion path and distribution of oxide particles with the particle trajectory model. In the model, a particle is released into the flow field, initially positioned at a point on the top surface. To statistically capture all probable scenarios of particle movement, several different axial and lateral input positions were examined with a uniform density of one particle per $0.5 \times 0.5 \text{ mm}^2$.

The workpiece moves with the welding velocity in the opposite direction, regarding the frame of reference attached to the welding torch. Therefore, as Fig. 1 shows, the workpiece material enters the domain from the inlet boundary and leaves the domain from the outlet surface. The top surface was exposed to the external heat input, i.e. the heat flux of the plasma arc that assumed to have a Gaussian distribution. All surfaces being cooled by air were subjected to convective heat transfer with the ambient environment. The boundary conditions of the domain are formulated in Table 1 and following equations:

$$q_{\text{arc}} = \eta \frac{VI}{\pi r_o^2} \exp[-\beta(x^2 + z^2)/r_o^2] \quad (16)$$

$$q_{\text{air}} = -H(T - T_o) \quad (17)$$

The heating power of the plasma arc was considered by Eq. (16) according to the electric current I , the voltage V and the electric efficiency η of the welding process. There might be about $\sim 10\%$ error in the total heat flux from the uncertainty in the efficiency. Because of complicated effects of the plasma arc and radiations, there are also uncertainties in the distribution of heat flux. The Gaussian function might have about $\sim 10\%$ error in describing the distribution of the actual heat flux. However, the model is widely used among researcher, since the heat flux could be adjusted with the spot size r_o and the distribution coefficient β to minimize the error. Consideration of the physics of plasma arc could be too costly for a 10% error in the distribution of heat flux. On the other hand, the focus of the current is the distribution of oxide particles, which is mostly affected by fluid flow. Thus, in the current study, the plasma arc was excluded from the calculation domain.

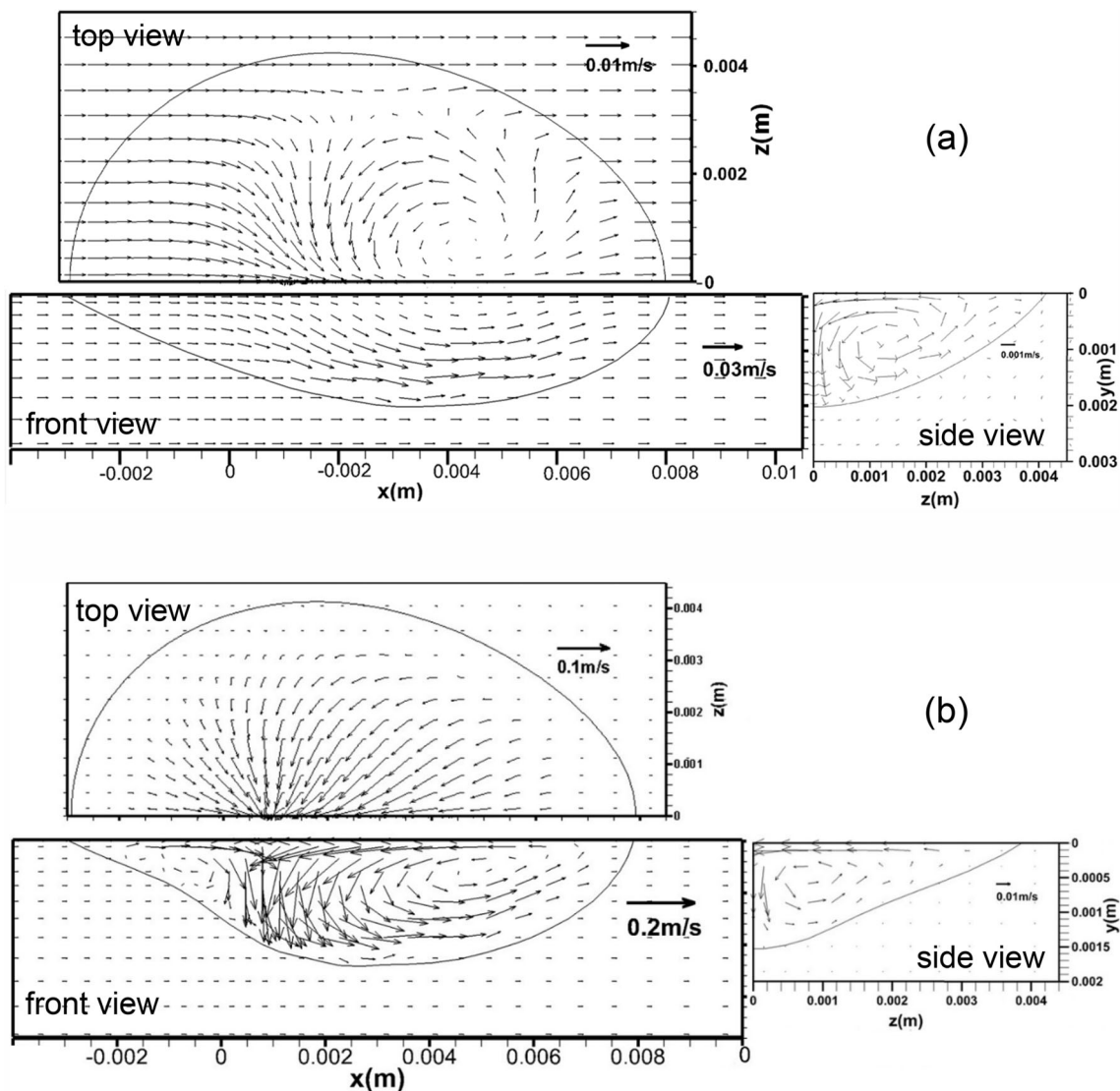


Fig. 5 Flow patterns formed in the weld pool. **a** Without Marangoni effect assuming the dominant force is electromagnetic (Lorentz) force. **b** With Marangoni effect (concentric surface tension gradients $\partial\gamma/\partial T > 0$)

Finite volume method (FVM) was used to discretize the governing equations in the model. This method allows for considering two-phase multi-physics of the welding problem with volume-averaging formulation in an efficient coarse grid. The computational domain was discretized to a number of non-uniform three-dimensional volume elements, regularly $45 \times 23 \times 15$ in x , y and z directions, respectively. To enhance the computational resolution, the computational grid was refined within the weld pool regions. The size of volume elements was refined to a minimum value of 0.03 mm^3 under the plasma arc. For time marching, a fully implicit constant time step of 0.01 s was adopted. The simulations were continued for a total real time about $\sim 5 \text{ s}$ to ensure a steady-state solution is obtained. The upwind scheme [26] was chosen to calculate convective values between nodes. SIMPLEC method was used to link the velocity and pressure field in the code. The phase change in the problem, i.e. solidification/melting, was numerically handled with enthalpy method. In the discretization of two-phase equations with phase change, cares were taken to get stable and consistent numerical setup [27]. For convergence, a criterion was set as if the summation of residuals of discretized equation for all nodes get smaller than 10^{-4} :

$$\sum_{\text{equations}} R = \sum_{\text{nodes}} |\sum a_{nb} \phi_{nb} + b - a_p \phi_p| \leq R_C \quad (18)$$

Figure 2 shows the general structure of the algorithm used in modelling. The material properties and process parameters used in the model are listed in Table 2. An open source CFD code in FORTRAN, called SENSE developed by Jafari [23] and verified and validated by Jafari et al. [27], was employed to conduct the numerical study. The simulations were executed on a Core-i7 7500U Intel laptop CPU engine which took about 6–24 h for each run depending on the grid sizes. All

simulations went with a good numerical stability and reached the convergence criteria defined.

3 Results and discussion

The numerical setup was firstly loaded in order to verify the model solutions. A-TIG welding was simulated in different grid densities of $40 \times 18 \times 12$, $45 \times 23 \times 15$, $50 \times 26 \times 18$ and $57 \times 29 \times 20$. Figure 3 shows the results of the grid dependency study. Temperature distribution, velocity field and shape of the pool have been chosen to be checked. In Fig. 3a, the distribution of temperature along the weld line shows a quite convergent trend. Maximum temperature of 2800 K has predicted in the pool with a sharp variation. The shape of weld pool in Fig. 3c has also been obtained with a stable geometry as the grid is refined. However, the axial velocity profile along the weld line, as shown in Fig. 3b, has appeared to be grid-dependent until the control volumes are refined to 0.02 mm^3 to reduce the discretization errors insofar less than 10%. Then, the numerical solution is found to be verified and the final grid spacing considered to be appropriate according to the acceptable error by Wang et al. [8].

Figure 4 illustrates the cross section of the welding pool from the numerical predictions against experimental picture. The shape of the pool was compared with the experimental micrographs of Tseng and Hsu [29] for TIG and A-TIG welding at a variety of oxygen content for 304L stainless steel. The depth-to-width ratio predicted to be 0.45 for TIG (Fig. 4a) where experiments shows a ratio of ~ 0.5 , i.e. an error of $\sim 10\%$ is present in numerical solution which is thought to be originated from mathematical description. Figure 4b shows the influence of oxygen content on the final weld shape during welding of AISI 304 stainless steel which is numerically

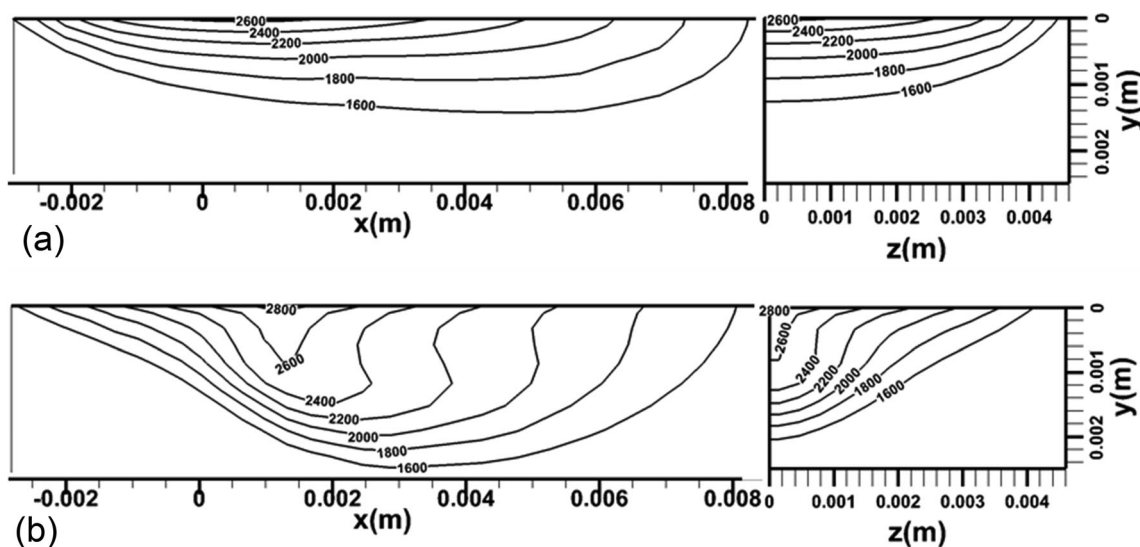


Fig. 6 Temperature distribution in transverse and longitudinal sections of the welding pool. a TIG. b A-TIG

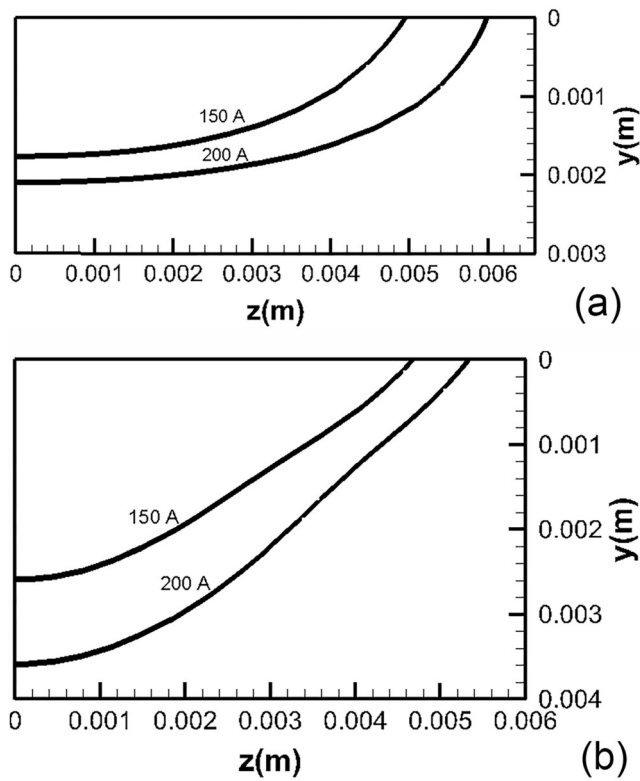


Fig. 7 Geometry of the weld pool under different welding currents. a TIG. b A-TIG

predicted with different surface tension gradients relevant to the oxygen contents. The addition of flux (oxygen content) revealed a significant increase in the weld depth (85%) due to flow pattern evolutions. Figure 5a displays vector plots of the weld pool velocity field, if there was no surface tension effect, i.e. without Marangoni force, where the dominant driving force is electromagnetic one. The same weld pool has been shown from different views in Fig. 5b after simulation with the Marangoni force applied. With a positive surface tension gradient, an inward concentric flow has been formed on top

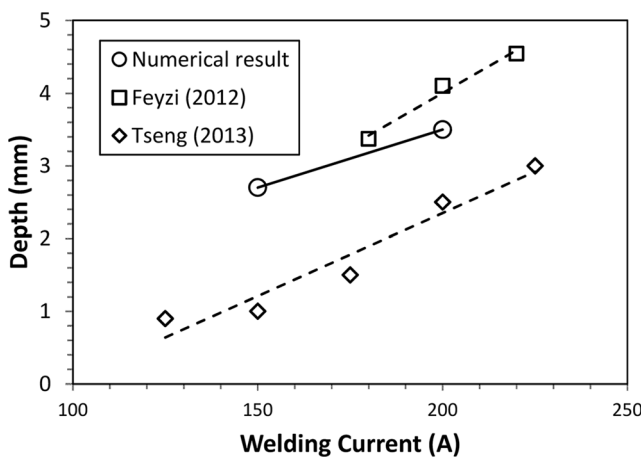


Fig. 8 Penetration depth of A-TIG welding of stainless steel at various currents

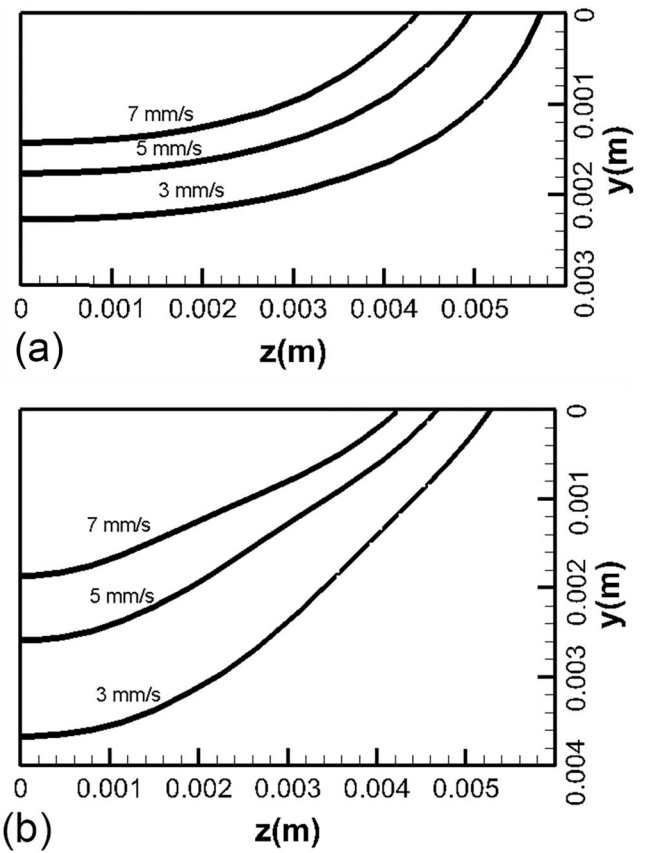


Fig. 9 Geometry of the weld pool with different welding velocities. a TIG. b A-TIG

layers of the weld pool, that causes heat swept and collected to warm up the hearth of the pool and consequently to enhance the pool dept. The relationship between changes in surface tension gradient of AISI 304SS and oxygen content was calculated according to Turquais’ [28] researches. The depth-to-width ratio for A-TIG welding was numerically predicted to be 0.7 where it has been reported to be 0.9 by Tseng [30] and Tseng and Hsu [29], i.e. there is a ~20% error in the numerical

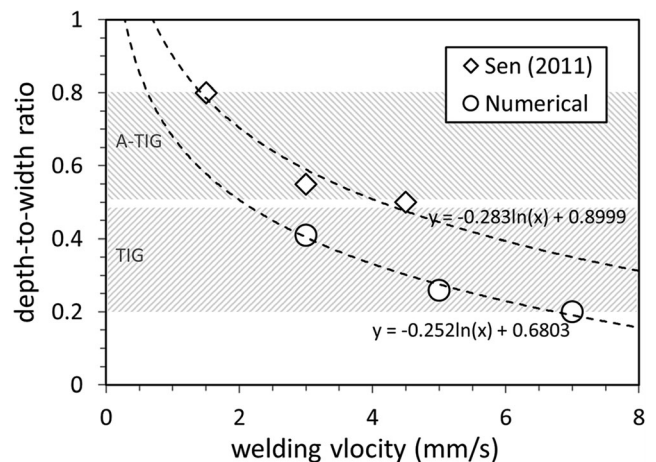


Fig. 10 Variation of depth-to-width ratio with welding velocity

solution that is related to the uncertainty in surface tension gradients.

A picture of the flow pattern of a weld pool with and without Marangoni effect can be seen in Fig. 5. The distribution of electric current density and electromagnetic force has been presented and discussed by Kumar and Debroy [24]. In the absence of Marangoni effects, simulations predict that the electromagnetic force would produce a flow pattern like the one shown in Fig. 5a. Two symmetrical horizontal circulation would form over the weld pool following the torch position and rolling the center line of the weld (one-half is seen in Fig. 5a). In the absence of Marangoni effect, the flow pattern would not show any circulation in the longitudinal section and the velocity of melt would reach to a maximum magnitude of 0.05 (m/s) in x direction. In the cross section, there would be a weak circulation. It is worthy reminding that the center of circulations has a lower pressure and there is a preferred place for low-density particles (e.g. oxides) to reside. Thus, a horizontal vortex as shown in Fig. 5a would hold the particles on the surface and prevent them to be immersed into the pool perhaps. In the presence of Marangoni effect however, with high thermal gradients and concentric surface tension gradients $\partial\gamma/\partial T > 0$ at top, the very upper films of atoms on the surface experience an asymmetric tension and accelerate toward the hot point. Therefore, the electromagnetic circulations vanish and a concentric flow pattern forms as plotted in Fig. 5b. In the longitudinal section, two asymmetric vertical circulations have appeared. A strong and expanded counter-clockwise vortex is following the position of the torch with a small clockwise vortex ahead at the nose of the weld pool. The maximum velocity of melt reaches ~ 0.2 m/s in the vertical direction deepening the pool. The center of the strong vertical vortex entraps oxide particles, a good reason why light-weight inclusions should plunge into a heavy molten metal. Furthermore, when additional particles join, they may become bigger in size and suddenly dragged and discharged out of the vortex to the solidifying back wall.

Figure 6 shows the iso-temperature contours obtained for transverse and longitudinal sections of the weld pool of TIG and A-TIG. The temperatures are above 2000 K in a big portion of the pool. At this high temperature with the presence of

active flux, low-size oxides are probably reduced, i.e. decomposing the particles and releasing oxygen could happen which would lead to a reversion in surface tension gradients. Then, the flow might be revolved toward center at higher temperatures (Fig. 5b) and the pool depth might be increased consequently (Fig. 6b). From the simulated results, it can be seen that temperatures as high as 2800 K in A-TIG and 2600 K in TIG are predicted with a same input power of welding torch and a same welding speed. It has been observed by Wu et al. [31] through an infrared thermometry that the mean peak temperature of the heat-affected zone (HAZ) was reasonably increased from 950 to 1100 °C when active coating was applied. The temperature dependence of surface tension then takes the role and alters the flow pattern which manages the heat flow to shape the weld pool according to the matter discussed for Fig. 5b.

Figure 7 demonstrates weld pool cross sections numerically obtained under different welding electric currents for both TIG and A-TIG. Gao and Wu [32] captured images of the weld pool and showed that an increased electric current provides more heat and expands the weld pool shape. Stadler et al. [33] have measured the amount of the expansion in TIG pool. However, it was remained unanswered how electric current influences the weld pool. In the present model, the electric current takes part in two places, the plasma arc heat flux and the electromagnetic force. The electromagnetic force introduces a squared order effect of electric current to flow pattern of the pool with Eqs. (6)–(8). The heat flux involves the electric current by Eq. (16). Figure 7b shows the expansion obtained in the shape of A-TIG pool which is somehow more in depth rather than in sideways, while TIG welding pool (Fig. 7a) shows it more in sideways. It reveals that the current has a different effect on the depth-to-width ratio in A-TIG, because of its contribution to the advection pattern. The penetration depth versus welding current has been summarized in a graph in Fig. 8 for three sets of results, present numerical predictions, experimental data reported by Feyzi [12] and by Tseng [30]. The graph indicates that the present model gives results nearby the measurements Feyzi [12] reported, but with the trend that Tseng [30] observed.

Table 3 Weld pool characteristics as function of welding parameters

Process		TIG					A-TIG			
Parameters	Current	(A)	150	150	150	200	150	150	150	200
	Speed	(mm/s)	3	5	7	5	3	5	7	5
Max. temperature (apprx.)		(K)	2700	2600	2500	2800	2900	2800	2700	3000
Depth/width ratio			0.43	0.4	0.33	0.38	0.73	0.7	0.5	0.8
Marangoni no.		Ma	3.3×10^5	3×10^5	2.6×10^5	3.6×10^5	4×10^5	3.6×10^5	3.3×10^5	4.3×10^5
Magnetic Reynold no.		Rm	1.4×10^5	1.4×10^5	1.4×10^5	2.2×10^5	1.4×10^5	1.4×10^5	1.4×10^5	2.2×10^5

Figure 9 displays how weld pool shape changes with the effect of welding velocity for TIG and A-TIG processes. As expected, increasing welding speed shrinks the weld pool because of shortening the accumulation of heat. However, the numerical investigation indicates there is a difference between what happens in TIG and A-TIG, as Fig. 9 shows. A significant variation has been predicted in the size of the pool, and

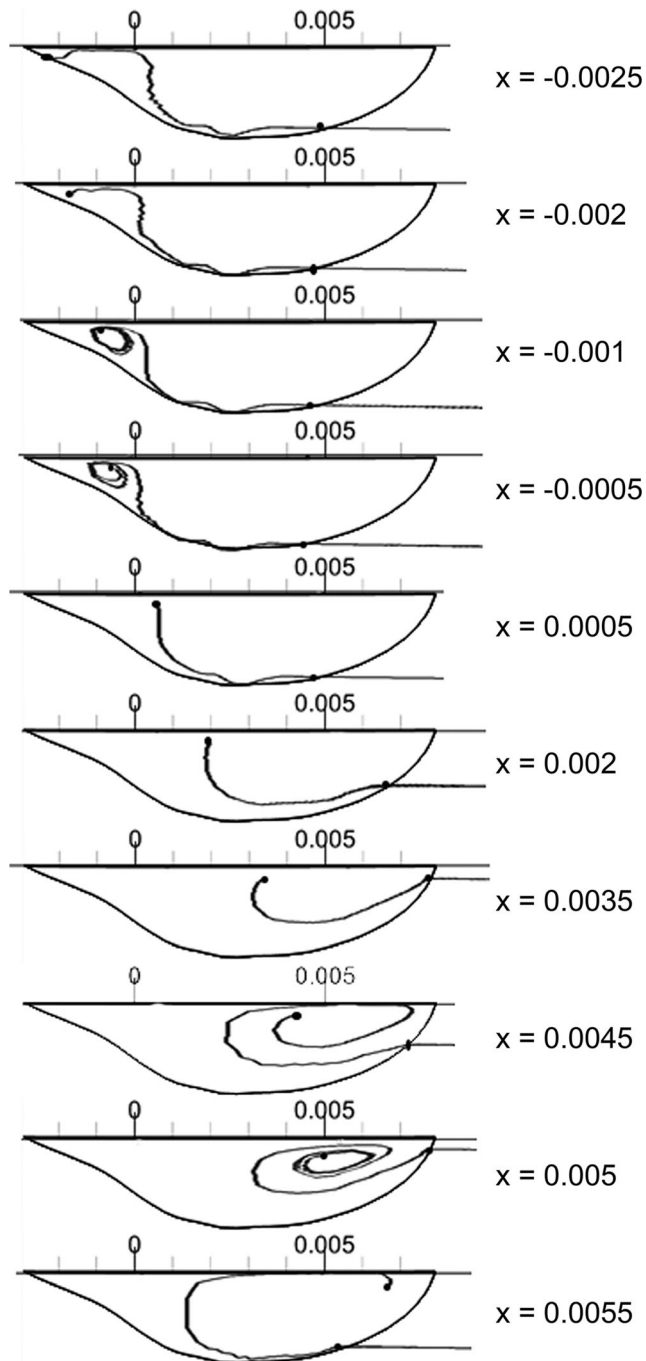


Fig. 11 Longitudinal section of the weld pool with trajectories of an oxide particle submerged into the weld pool from different locations on the weld line. The welding torch is positioned at 0 (m) and the direction of welding is right-to-left. All dimensions are in (m)

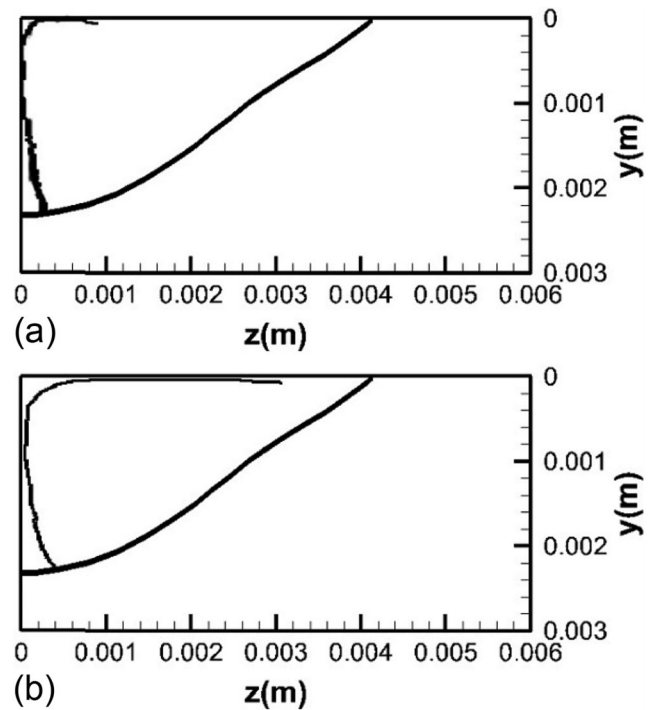


Fig. 12 The cross section of the weld pool just under the torch showing trajectories of an oxide particle submerged into the pool from different locations. All dimensions are in (m)

there is not a considerable change in the form of the pool in TIG. In a contrary, variations in the welding speed of A-TIG process not only change the size of the pool but also alter the form of it, i.e. the aspect ratio and angles have been shifted in Fig. 9b toward the form of TIG welding pool. To validate and clarify the issue, variations of aspect ratio with welding speed have been collected in Fig. 10 from the numerical results in comparison with experimental observations by Sen et al. [34]. Both sets of results show that there is a reduction in the aspect ratio of the pool with increasing the welding speed. That

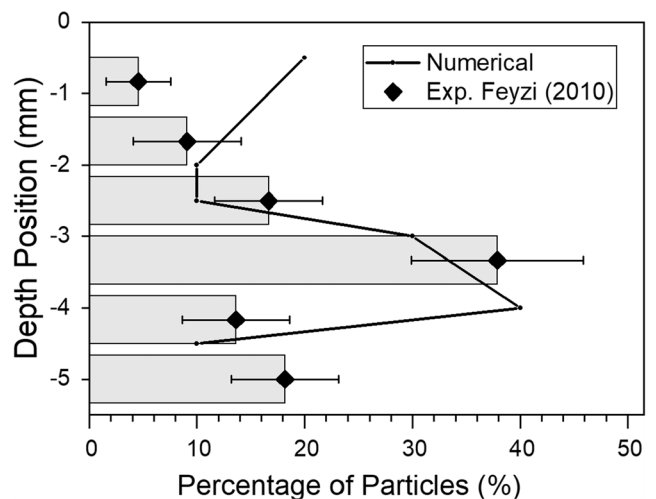


Fig. 13 Distribution of particles entrapped in the cross section of A-TIG weld line; numerical results in comparison with experimental data collected from metallographic observations by Feyzi [12]

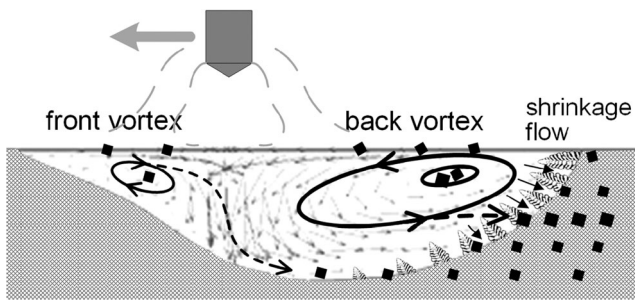


Fig. 14 Schematic of the flow pattern and particle motion path in the A-TIG weld pool, explaining how particles are disturbed as shown in Fig. 13

means, for someone who wants to speed up the A-TIG process for productivity, there is probably a limit of welding speed, beyond which the depth-to-width ratio would be declined below the requirements of the process and the welding practice could fail. In other words, an A-TIG process would be degraded to a TIG-like performance if welding speed exceeds a critical limit.

Table 3 provides a summary of the results obtained from a parametric study of TIG and A-TIG simulations. Magnetic Reynolds numbers (R_m) and Marangoni numbers (Ma) are presented, relatively evaluating the impact of electromagnetic force and surface tension on the formation of weld pools. From the results, it was found out that A-TIG is generally more sensitive than TIG to the process parameters. Furthermore, Marangoni numbers are about twice the magnetic Reynold numbers, pointing out that the surface tension has a dominant effect on the weld pool configurations.

The computed flow field was used to investigate motion path and distribution of oxide particles with the particle trajectory model. In the model, a particle was released into the flow field,

Fig. 15 Variations of vertical force along with longitudinal distance on the surface of weld pool for particles with different diameters

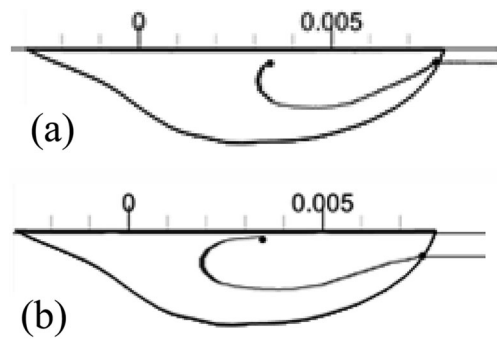
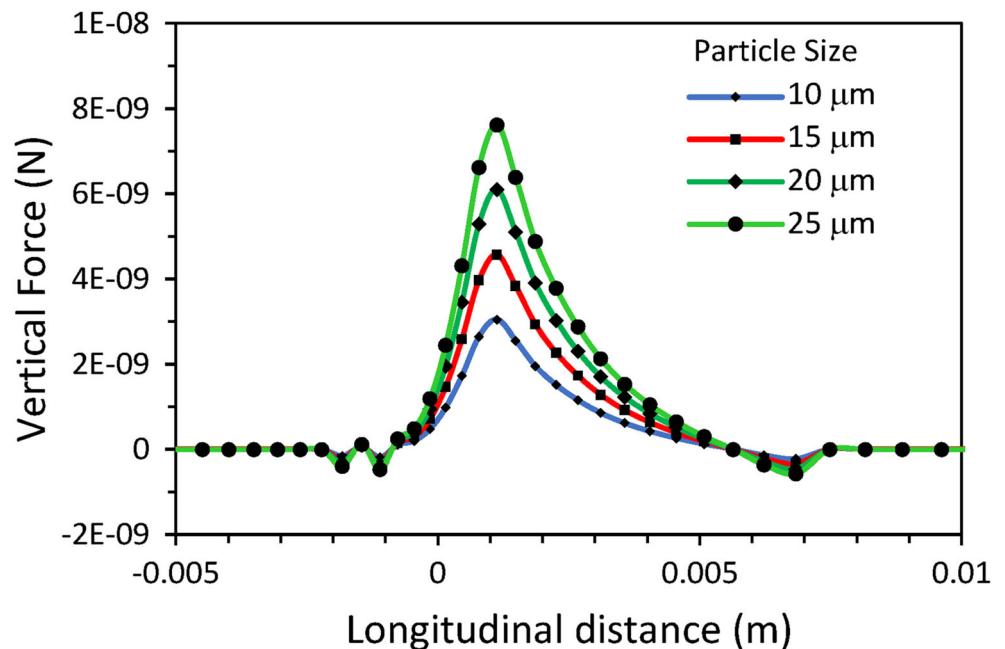


Fig. 16 Trajectories of two oxide particles with different sizes released at $x = 3.5$ mm. **a** $D = 10 \mu\text{m}$. **b** $D = 20 \mu\text{m}$

initially positioned at a point on the top surface. Several different axial and lateral positions were examined with a uniform density of 4 particles per millimeter to statistically capture all probable scenarios of particle movement. Figure 11 and Fig. 12 illustrate a selected set of trajectories obtained for the particles. From the cross section view in Fig. 12, it was found that, no matter where a particle is released from, the Marangoni convection picks the particle and takes it to the center of the pool. Almost all oxide particles bigger than $\sim 10 \mu\text{m}$ were predicted to be immersed in the hot part of the welding pool. Figure 11 shows that the final journey of seven, out of ten, particles has ended with an entrapment in higher depths of the weld line. Figure 13 shows a relative distribution of particles achieved by numerical simulations in comparison with collected experimental data from metallographic investigations by Feyzi [12]. The experimental bar chart approves that about 70% of particles are entrapped in the deeper half of cross section of the weld line. Regarding the numerical motion paths in Fig. 11, four particles have gone through vortex traps. Two of them were caught by the front vortex and another

two were taken by the intense vortex in the back (according to Fig. 5b and the direction of welding, there are two vortices in the weld flow pattern, namely, the front and the back). The path of particles, caught by the front vortex, has been ended at the highest depth observed. However, those trapped by the back vortex have been released in the middle depth. So far we know, since metal vortices produce low pressure centers, they have a strong potential to capture and collect low-density oxide particles. The more intense the vortex is, the more particles would be trapped and the bigger they could be in size. Therefore, it is the back vortex as the main feature in the flow pattern of A-TIG pool that is responsible to explain why distributed oxide particles are frequently observed in the deeper half of joint cross section. Figure 14 illustrates that explanation. The back vortex picks most of the particles from a big portion of top surface behind the torch, and discharges them to the lower half of back wall of the weld pool. The back wall is mushy and dendritic (high thermal gradients stimulate interface instability and dendritic solidification). In the vicinity of the back wall, the dominant flow is a shrinkage flow toward the wall due to solidification and different densities of solid and liquid. As soon as a particle comes close to touch the wall, it is pulled by shrinkage flow and grasped by growing dendrites. There are chances for a particle at the bottom of the pool to return to the bulk flow circulation, because the rate of solidification and therefore the intensity of shrinkage flow are ignorable at the bottom. However, at the middle regions of the back wall, the shrinkage flow appears in its maximum rate and the Marangoni convection also coporates to deliver the particles to the wall. That is how most of the particles have a trajectory ended up to a middle depth entrapment.

Beside the distribution of particles, mechanical behavior of the welded joint concerns to find out where bigger size particles do accumulate. From the numerical investigations, it was found that the size of particles would also influence their motion paths (see Eqs. (14) and (15)). Figure 15 shows the variations of vertical force applied to the particle along with axial direction on surface of the pool for different particle sizes. With the radius of the particle being increased, the magnitude of the submerging force has been increased with a similar trend. Figure 16 shows motion tracking for two particles with 10 and 20 microns in diameter. It can be seen that the bigger particle would experience a bigger drag force from the flow field and be entrapped in a deeper position in the weld. Feyzi [12] reported macrographs of the cross section of weld showing that big-sized particles have often observed in the middle depth of the weld.

4 Conclusions

A three-dimensional numerical model was developed predicting weld pool shape, temperature distributions, flow

patterns and motion paths of immersing oxide particles for A-TIG welding of 304L stainless steel. The following concluding remarks can be drawn:

1. The highest temperature of the pool was predicted to be 2600 K for TIG and 2800 K for A-TIG. The depth-to-width ratio (d/w) was 0.4 and 0.7 for TIG and A-TIG, respectively.
2. Marangoni and magnetohydrodynamic effects have the main contribution to form the flow field and the shape of welding pool of A-TIG, while Marangoni force is two times more influential than electromagnetic force. The main features of the flow pattern were predicted to be two vortices, one in the front and another in the back of arc location. The bigger and stronger vortex in the back, with velocities reached up to ~ 0.2 m/s in vertical direction under the arc, promotes depth-to-width ratio and causes particle entrapments however.
3. Based on simulation results, increasing the electric current in TIG welding showed more lateral expansion in the weld pool and did not enhance the depth-to-width ratio. However, in A-TIG, a 33% increase in the current was predicted to give 14% increase in depth-to-width ratio. Welding speed effectively changed the size of the pool in TIG, while for A-TIG, not only it changed the size but also it altered the form of the pool, i.e. increasing the speed of A-TIG shifts the aspect ratio and angles of welding pool toward the form of those for TIG. Therefore, there might be a critical limit of welding speed in A-TIG process beyond which the depth-to-width ratio would be declined below the requirements and the welding practice could be degraded to a TIG-like performance.
4. Numerical results for trajectories of oxide particles showed that particles were often dragged, submerged and entrapped in the weld pool. Between many particles released from different positions of top surface, about 70% have had a trajectory ended at the deeper half of cross section of the weld. It is somehow consistent with the previous metallographic observations by Feyzi [12] on the distribution of particles in cross section of A-TIG weld.
5. The reason for the obtained distribution of particles in the cross section is thought to be the function of back vortex in flow regime of the pool. The back vortex picks most of the particles from a big portion of top surface behind the arc, immerses them into the pool and delivers and discharges them to the lower half of pool back wall. Near the back wall where the solidification rate is high, shrinkage flow drags the particles and dendritic wall grasps them within the mushy structure of the solidifying weld.

Acknowledgements The authors would like to acknowledge the Department of Materials and Metallurgical Engineering at Amirkabir University of Technology. This research did not receive any specific grant from funding agencies in the public, commercial or not-for-profit sectors.

Nomenclature Letters a , acceleration (m/s^2); B , magnetic field (T); c , specific heat (J/kgK); D , particle diameter (m); F , force (N); f , mass fraction; H , heat transfer coefficient ($\text{W/m}^2 \text{K}$); h , enthalpy (J/kg); I , welding current (A); J , current density (A/m^2); k , thermal conductivity (W/mK); K , permeability (m^2); K_o , porosity constant (m^2); L_f , latent heat of fusion (J/kg); L_1 , length of sheet (m); L_2 , thickness of sheet (m); L_3 , width of sheet (m); m , mass (kg); Ma , Marangoni number; P , pressure (Pa); q , heat flux (W/m^2); r , radial position (m); r_o , effective arc radius (m); R , residual of the solution; R_m , magnetic Reynold number; S , enthalpy source term (W/m^3); T , temperature (K); T_o , environment temperature (K); t , time (s); u , velocity in x direction (m/s); v , velocity in y direction (m/s); V , welding voltage (V); w , velocity in z axis direction (m/s); x , x position (m); y , y position (m); z , z position (m)

Greek letters γ , surface tension (J/m^2); τ_M , Marangoni surface tension (Pa); β , arc distribution factor; η , arc efficiency; μ , dynamic viscosity (kg/ms); μ_m , magnetic permeability (wb/Am); ρ , density (kg/m^3)

Superscripts D , Darcy; EMF, electromotive force; M , Marangoni force

Subscripts cooling, cooling wall; D , drag; G , gravity; heating, heating wall; L , Liquidus; p , particle; S , Solidus; W , welding

References

- Messler RW (1999) Fusion welding processes. Principles of welding. In: Wiley Online Books, pp 40–93
- Modenesi PJ, Apolin R, Pereira IM (2000) TIG welding with single-component fluxes. *J Mater Process Technol* 99:260–265
- Heiple CR, Roper JR (1982) Mechanism for minor element effect on GTA fusion zone geometry. *Weld J* 61:975–1025
- Zhao YZ, Zhao HY, Lei YP, Shi YW (2007) Theoretical study of Marangoni convection and weld penetration under influence of high oxygen content in base metal. *Sci Technol Weld Join* 12: 410–417
- Zhao CX, Kwakernaak C, Pan Y, Richardson IM, Saldi Z, Kenjeres S, Kleijn CR (2010) The effect of oxygen on transitional Marangoni flow in laser spot welding. *Acta Mater* 58:6345–6357
- Li D, Lu S, Dong W, Li D, Li Y (2012) Study of the law between the weld pool shape variations with the welding parameters under two TIG processes. *J Mater Process Technol* 212:128–136
- Li C, Shi Y, Gu Y, Fan D, Zhu M (2018) Effects of different activating fluxes on the surface tension of molten metal in gas tungsten arc welding. *J Manuf Process* 32:395–402
- Wang X, Huang J, Huang Y, Fan D, Guo Y (2017) Investigation of heat transfer and fluid flow in activating TIG welding by numerical modeling. *Appl Therm Eng* 113:27–35
- Berthier A, Paillard P, Carin M, Valensi F, Pellerin S (2012) TIG and A-TIG welding experimental investigations and comparison to simulation, Part 1: identification of Marangoni effect. *Sci Technol Weld Join* 17:609–615
- Vidhyarthi RS, Dwivedi DK (2016) Activating flux tungsten inert gas welding for enhanced weld penetration. *J Manuf Process* 22:211–228
- Aucott L, Dong H, Mirihanage W, Atwood R, Kidess A, Gao S, Wen S, Marsden J, Feng S, Tong M, Connolley T, Drakopoulos M, Kleijn CR, Richardson IM, Browne DJ, Mathiesen RH, Atkinson HV (2018) Revealing internal flow behaviour in arc welding and additive manufacturing of metals. *Nat Commun* 9:5414
- Feyzi F (2012) Study of effective factors on distribution of the oxide particles in A-TIG weld pool of 304L stainless steel. Sahand University of Technology, Sahand
- Jaidi J, Dutta P (2004) Three-dimensional turbulent weld pool convection in gas metal arc welding process. *Sci Technol Weld Join* 9:407–414
- Yushchenko KA, Kovalenko DV, Krivtsun IV, Demchenko VF, Kovalenko IV, Lesnoy AB (2009) Experimental studies and mathematical modelling of penetration in TIG and A-TIG stationary arc welding of stainless steel. *Weld World* 53:R253–RR63
- Crowe C, Michaelides E, Schwarzkopf JD (2016) Multiphase flow handbook, 2nd edn. Mechanical and aerospace engineering series. CRC Press, Boca Raton
- Miki Y, Thomas BG (1999) Modeling of inclusion removal in a tundish. *Metall Mater Trans B* 30:639–654
- Horwitz J, Mani A (2016) Accurate calculation of Stokes drag for point-particle tracking in two-way coupled flows. *J Comput Phys* 318:85–109
- Mahanthesh B, Gireesha BJ (2018) Thermal Marangoni convection in two-phase flow of dusty Casson fluid. *Results Phys* 8:537–544
- Murphy AB (2015) A perspective on arc welding research: the importance of the arc, unresolved questions and future directions. *Plasma Chem Plasma Process* 35:471–489
- Hong C-P (2004) Computer modelling of heat and fluid flow in materials processing. IOP Publishing Ltd., Bristol
- Iida T, Guthrie RIL. The physical properties of liquid metals: Oxford : Clarendon press; 1988.
- Pop I, Postelnicu A, Groşan T (2001) Thermosolutal Marangoni forced convection boundary layers. *Meccanica* 36:555–571
- Jafari A (2011) Modeling of solidification structure evolution and macrosegregation in direct-chill casting of aluminum alloys. Iran University Of Science and Technology, Tehran
- Kumar A, Debroy T (2003) Calculation of three-dimensional electromagnetic force field during arc welding.
- Chen K (2007) Micro Particle Transport and deposition in human upper airways. Publisher, Seattle
- Patankar SV (1980) Numerical heat transfer and fluid flow. Hemisphere Publishing Corporation, New York
- Jafari A, Seyedein SH, Aboutalebi MR (2011) Semi-implicit method for thermodynamically linked equations in phase change problems (SIMTLE). *Appl Math Model* 35:4774–4789
- Turquais B (2017) Influence of the steel properties on the progression of a severe accident in a nuclear reactor. CEA Cadarache, Saint Paul Lez Durance
- Tseng K-H, Hsu C-Y (2011) Performance of activated TIG process in austenitic stainless steel welds. *J Mater Process Technol* 211: 503–512
- Tseng K-H (2013) Development and application of oxide-based flux powder for tungsten inert gas welding of austenitic stainless steels. *Powder Technol* 233:72–79
- Wu B, Wang B, Zhao X, Peng H (2018) Effect of active fluxes on thermophysical properties of 309 L stainless-steel welds. *J Mater Process Technol* 255:212–218
- Gao J, Wu C (2001) Experimental determination of weld pool geometry in gas tungsten arc welding. *Sci Technol Weld Join* 6:288–292
- Stadler M, Masquere M, Freton P, Gonzalez JJ (2017) Experimental characterisation of the weld pool expansion in a tungsten inert gas configuration. *Sci Technol Weld Join* 22:319–326
- Sen D, Ball KS, Pierson MA (2011) Numerical investigation of transient Marangoni effects on weld pool dynamics in gas tungsten arc welding of stainless steel. IMECE2011: Publisher.

Publisher's note Springer Nature remains neutral with regard to jurisdictional claims in published maps and institutional affiliations.